*minerals*

MDPI

*Article*

# Mechanical Properties of Differently Nanostructured and High-Pressure Compressed Hydroxyapatite-Based Materials for Bone Tissue Regeneration

**Vijay H. Ingole [1,2,3,*], Shubham S. Ghule [1], Tomaž Vuherer [3], Vanja Kokol [3,*] and Anil V. Ghule [1,2,*]**

[1] Department of Chemistry, Shivaji University, Kolhapur 416004, India; ghuleshubham121013@gmail.com
[2] Department of Nanotechnology, Dr. Babasaheb Ambedkar Marathwada University, Aurangabad 431004, India
[3] Faculty of Mechanical Engineering, University of Maribor, 2000 Maribor, Slovenia; tomaz.vuherer@um.si
* Correspondence: mvt.vijay@gmail.com (V.H.I.); vanja.kokol@um.si (V.K.); avg_chem@unishivaji.ac.in (A.V.G.)

**Abstract:** Hydroxyapatite (HAp) has long been considered the gold standard in the biomedical field, considering its composition and close resemblance to human bone. However, the brittle nature of hydroxyapatite (HAp) biomaterial, constrained by its low fracture toughness (of up to 1.2 vs. 2–12 MPa $m^{1/2}$ of human bone), remains one of the significant factors impairing its use in bone regeneration. In the present study, HAp nanoparticles synthesized by the solid-state (SHAp) and sonochemical (EHAp) approaches using eggshell-derived calcium hydroxide and ammonium dihydrogen orthophosphate as precursors are compared with those synthesized using commercially available calcium hydroxide and ammonium dihydrogen orthophosphate as precursors (CHAp) employing sonochemical method. The HAp samples were then compressed into compact materials using a uniaxial high-pressure compression technique at a preoptimized load and subsequently characterized for mechanical properties using the Vickers indentation method and compressive strength testing. The analysis revealed that the material with smaller particle size (30–40 nm) and crystalline nature (EHAp and CHAp) resulted in mechanically robust materials ($\sigma_m$ = 54.53 MPa and 47.72 MPa) with high elastic modulus (E = 4011.1 MPa and 2750.25 MPa) and density/hardness-dependent fracture toughness ($\sigma_f$ = 4.34 MPa $m^{1/2}$and 6.57 MPa $m^{1/2}$) than SHAp ($\sigma_m$ =28.40 MPa, E = 2116.75 MPa, $\sigma_f$ = 5.39 MPa $m^{1/2}$). The CHAp material was found to be the most suitable for applications in bone regeneration.

**Keywords:** bone regeneration; hydroxyapatite; nanoparticles; compression; mechanical properties

check for updates

**Citation:** Ingole, V.H.; Ghule, S.S.; Vuherer, T.; Kokol, V.; Ghule, A.V. Mechanical Properties of Differently Nanostructured and High-Pressure Compressed Hydroxyapatite-Based Materials for Bone Tissue Regeneration. *Minerals* **2021**, *11*, 1390. https://doi.org/10.3390/min11121390

Academic Editors: Josy A. Osajima, Edson Cavalcanti da Silva Filho and Maria Gardennia Fonseca

Received: 22 October 2021
Accepted: 4 December 2021
Published: 8 December 2021

**Publisher's Note:** MDPI stays neutral with regard to jurisdictional claims in published maps and institutional affiliations.

**Copyright:** © 2021 by the authors. Licensee MDPI, Basel, Switzerland. This article is an open access article distributed under the terms and conditions of the Creative Commons Attribution (CC BY) license (https://creativecommons.org/licenses/by/4.0/).

## 1. Introduction

Hydroxyapatite ($Ca_{10}(PO_4)_6(OH)_2$, HAp) is a biomedical-grade ceramic that is widely used in bone repair and replacement [1]. The exceptional biological properties of HAp, such as nontoxicity, biocompatibility, and, most importantly, bioactivity result from its chemical composition which is similar to that of natural bone [2,3]. Moreover, the biocompatibility of HAp allows it to be used for a variety of applications inside the human body, including bone regeneration, drug delivery, and cell imaging [4–6]. A bone substitute material must include mechanical strength that is as close as possible to the natural bone [7,8]. However, HAp has lower mechanical strength than the natural bone, and thus, it remains a critical challenge which limits its application for load-bearing applications [9,10].

Bone comprises two distinct forms, inner porous cancellous bone and outer dense cortical bone, with unique histological and mechanical properties (strength, resilience, and flexibility). Thus, cancellous bone has a lower Young's modulus and is more elastic than cortical bone [11,12]. The biomechanical properties are a crucial factor in designing a bone graft biomaterial for replacement. Besides its geometry [13], the material must be mechanically robust and biocompatible with the damaged bone tissue to cope with the complex stress environment at the tissue site, acting as mechanical support until

new tissue is generated to withstand the mechanical load [13–15]. Thus, developing hydroxyapatite-based scaffolds and bone graft with improved load-bearing properties for bone regeneration is a current need [16]. The nanoscale Hap, by virtue, has high surface area, nanocrystalline nature, optimized sinterability, and desired densification, which enhances fracture toughness and other mechanical properties, and thus is favorable for bone regeneration application [17]. The mechanical properties of nanoscale HAp have been reported to be superior to its microscale counterpart, and thus, extensive study is focused on improving the properties of nanoscale HAp for its envisaged applications in bone tissue engineering [18–21].

Autografts containing a patient's living cells and growth factors are still the gold standard, although the autografts have several limitations arising from calcium phosphates, bioactive composites, growth factors [8], and alternative allografts (using a donor's bone). Furthermore, there are limited sources and supplies of bone, and the loss of biological factors and strength following demineralization are causes of great concern.

It eventually increases their elastic modulus and leads to low-stress shielding during a long implantation time, causing a failure of bone repair [13,22]. Besides this, there are concerns regarding the immunological reactions of such materials and disease transmission, which may cause unpredictable healing [23].

Because of the above drawbacks, there is still an increasing demand for synthetic bone material as a substitute to natural bone, including metals [24], polymers [13,14], and bioceramics (such as calcium phosphate, calcium sulphate, b-tricalcium phosphate, and HAp powders, granules, or porous blocks), also acting as a carrier for drug or gene delivery [18,25–27]. Among them, calcium orthophosphate ceramics, particularly HA, have attracted significant attention due to their excellent biological behavior, such as biocompatibility, bioactivity, and osteoconductivity. However, its brittle nature (constrained by the low fracture toughness (0.8–1.2 MPa $m^{1/2}$) and low flexural strength (<140 MPa)) limits its technological applications [25]. In general, the mechanical properties decrease significantly with the increasing content of an amorphous phase, microporosity, and grain sizes. On the other hand, high crystallinity, low porosity, and small grain sizes impart higher stiffness, higher compressive and tensile strength, and more excellent fracture toughness. However, fracture toughness is one of the essential properties which describes the ability of a material containing a crack to resist fracture, which still does not exceed the value of ~1.2 MPa·$m^{1/2}$ (human bone: 2–12 MPa·$m^{1/2}$). Moreover, it decreases almost linearly with increased porosity and increases with a decrease in grain size [15].

Many attempts have been made to prepare HAps at the nanoscale [18,28–30], including mechanochemical synthesis [31], combustion and various wet chemical techniques [32], molten salt preparation, and hydrothermal synthesis [33]. However, the sonochemical method, which is based on the chemical reaction activated by ultrasound radiation [34,35], has been reported as the most suitable for the production of uniform, small-sized, and pure HAp nanosized crystals with the least agglomeration and a higher surface area, resulting in an enhancement of the sintering kinetics and, consequently, improved mechanical properties of the bioceramics [36,37].

High-pressure compaction and sintering at high temperature are the typical approach to attain augmented mechanical properties of Hap-based bioceramic. However, the sintered material becomes porous, tends to lose its uniformity, and develops cracks. Moreover, sintering at elevated temperatures often changes the HAp phase and affects the mechanical properties [38]. For example, it tends to eliminate the hydroxyl functional groups in the HAp. Thus, it may result in the decomposition of the HAp phase to form α-tricalcium phosphate (α-TCP), β-tricalcium phosphate (β-TCP), and tetra calcium phosphate (TTCP) [26], thereby deteriorating the biocompatibility of synthesized HAp.

Our previous investigation on the in vitro biocompatibility of this material revealed that it is highly biocompatible and bioactive against hFOB cells [39,40] Thus, this study aims to evaluate the complex mechanical properties of the biomaterials prepared from differently presynthesized HAp nanoparticles by the high-pressure compression technique,

under controlled parameters and at ambient temperature. Since the HAp powders were to be thermally pretreated at 900 °C, it was expected that the compression techniques to form such biomaterials would not affect the crystalline or chemical structure of HAp. Therefore, it would be more appropriate to relate to the mechanical properties required for bone regeneration applications to develop bone grafts and scaffolds in load-bearing applications. The HAp nanoparticles were synthesized using different sources (eggshell-derived calcium vs. chemical precursors) and synthesis approaches (the solid-state and sonochemical).

Furthermore, to obtain the balanced compression strength and fracture toughness, the preparation of such HAp-based materials is first optimized related to the applied compression load using the Vickers indentation method [38,41–43]. The compression strength, fracture compression strength, yield compression strength, shrinkage, and Young's elastic modulus [44–46] of different nanostructured materials are then recorded and compared to better understand the contributions of nanoscale features using different types of HAp nanoparticles.

## 2. Experimental

### *2.1. Materials*

Eggshells procured from local vendors were used as a calcium precursor. In addition, ammonium hydroxide ($NH_4OH$), ammonium dihydrogen orthophosphate ($NH_4H_2PO_4$), hydrogen peroxide ($H_2O_2$), and calcium hydroxide ($Ca(OH)_2$) were obtained from Fisher Scientific, Aurangabad, India. All the reagents procured were analytical grade and used without further purification.

### *2.2. Synthesis of Hydroxyapatite (HAp) Nanoparticles*

Hydroxyapatite (HAp) nanoparticles were prepared by using CaO derived from eggshells as the calcium source and $NH_4H_2PO_4$ as a phosphorus precursor by two different methods, i.e., solid-state synthesis (SHAp) and sonochemical synthesis (EHAp). In addition, a similar synthesis of HAp was also performed using reagent grade $Ca(OH)_2$ and $NH_4H_2PO_4$ as a phosphorus precursor, referred to as (CHAp). Our previous work has presented the preparation of CaO from eggshells and its conversion into $Ca(OH)_2$ [39]. Briefly, the eggshells were crushed and washed with deionized water, followed by ultrasonication in 25% $v/v$ of Milli-Q water, and dried in an oven at 100 °C for 2 h. The obtained material was ground coarsely in a mortar–pestle and then subjected to ball milling (RETSCH-PM 100) to obtain a fine powder. To obtain a fine powder, the ground eggshell powder was ball-milled at 200 rpm for 30 min initially and then at 400 rpm for 1 h. Subsequently, the powder was calcined at 900 °C for 2 h with 200 °C intervals to decompose the organic matter and convert the $CaCO_3$ into CaO. Finally, the powder obtained was mixed with $NH_4OH$ and ultrasonicated for 1 h to form $Ca(OH)_2$.

Furthermore, HAp nanoparticles were synthesized by solid-state reaction (SHAp) and also by the sonochemical method (EHAp), using 1.23 g of $Ca(OH)_2$ (obtained from eggshells) and 1.15 g of $NH_4H_2PO_4$, corresponding to a stoichiometric ratio of Ca/P = 1.67. In the case of SHAp preparation, the compounds were ground in an agate mortar and pestle to obtain a homogenized mixture before being kept in a furnace box at 900 °C for 2 h. In EHAp preparation, the ground mixture was dissolved in 50 mL of deionized water and heated on a magnetic stirrer for 15 min, followed by ultrasonication for 1 h and heating further on a magnetic stirrer to evaporate the water. Finally, the product was ground in an agate mortar pestle to obtain the fine powder. Similarly, the synthesis of HAp using reagent grade $Ca(OH)_2$ and $NH_4H_2PO_4$ as precursors by ultrasonication (CHAp) was also performed for comparison.

### *2.3. Characterization of HAp Nanoparticles*

The samples were analyzed by X-ray powder diffraction (XRD; D8 ADVANCE BRUKER, Billerica, MA, USA, in reflection mode with Cu $K\alpha_1$ radiation. The average crystallite size of the HAp powder was also estimated using Scherrer's formula:

$t_{(hkl)} = 0.9\ \lambda/B\ Cos\theta_{(hkl)}$ [39,47], where "$\lambda$" is the wavelength of the monochromatic X-ray beam, $B$ is the full width at half maximum (FWHM) of the peak at the maximum intensity, $\theta$ is the peak diffraction angle and satisfies Bragg's law for the ($h\ k\ l$) plane, $t$($h\ k\ l$) is the crystallite size, and $\lambda$ is the wavelength of the X-rays ($\lambda$ = 1.54056 Å for Cu K$\alpha_1$ radiation).

The infrared (IR) spectra were recorded over the region 400–4000 cm$^{-1}$ and with the spectral resolution of 4 cm$^{-1}$ by Fourier transform infrared spectroscopy (FTIR, CARRY 600 Series, Tokyo, Japan), using the ATR technique. The morphology of the samples was analyzed by a scanning electron microscope (SEM) using Hitachi S4800, Tokyo, Japan, operated at 20 kV with images taken at various magnifications from 5 k to 200 k. To circumvent the charging effect, prior to the analysis, the samples were coated with an epitaxial thin Au layer using a Hitachi E1010 Ion sputter, Tokyo, Japan.

### *2.4. Preparation and Mechanical Testing of Pellet Materials from HAp Nanoparticles*

The pellets were prepared using powders of differently presynthesized HAp nanoparticles (SHAp, EHAp, and CHAp) under high pressure by the uniaxial compression technique (Smitweld Thermal Cycle Simulator TCS 1405 Smitweld b.v. (now Lincoln Smitweld b.v.), Nijmegen, The Netherlands) in which force, velocity, and displacement were controlled and measured by the tensile testing unit (Smitweld Thermal Cycle Simulator TTU 2002 Smitweld b.v. (now Lincoln Smitweld b.v.), Nijmegen, The Netherlands).

The force versus displacement and stress versus displacement data were recorded for each pellet. Two cylindrical pellets were prepared, with a diameter of 5 mm. A total of 100 mg weighted pellets were used for the Vickers hardness tests and fracture toughness tests, while 200 mg weighted pellets were used for the compression tests. Both types of pellets were used for density evaluation, which was investigated by measuring the mass of each pellet on a digital weighing machine while taking into account its geometry, measured by a Vernier caliper. In order to obtain the balanced compression strength and fracture toughness, the preparation of such materials is first optimized related to the applied compression load using the Vickers indentation method [42] and SHAp sample. For that purpose, a diamond indenter [43] is used to make an impression of a small crack on the sample specimen. Then, by inspecting the morphology of these cracks, the hardness and fracture toughness of the specimen [37,43] is studied. The complex mechanical properties (compression strength, fracture compression strength, yield compression strength, shrinkage, Young's elastic modulus) [36] of differently nanostructured materials are then recorded and compared at preoptimized conditions.

### *2.5. Statistical Analysis*

The results are presented as representative data or mean ± SD values of at least three independent experiments. The differences between treatments were analyzed by analysis of variance (ANOVA) with Tukey's multiple comparison tests (density, hardness, yield strength, compression strength, and fracture toughness), and the Kruskal–Wallis nonparametric test (the shrinkage and elastic modulus), respectively, using SPSS software (IBM SPSS 25, Armonk, NY, USA). All tests were with a significance level of $p < 0.05$. Therefore, there was a statistically significant difference in the mean value of different samples (SHAp, CHAp, and EHAp).

## 3. Results and Discussion

### *3.1. Characterization of Synthesized HAp*

Different analytical methods were used to characterize the structure and morphology of the synthesized HAp. The FTIR spectra of SHAp, EHAp, and CHAp samples are shown in Figure 1. It is observed that the spectra of the whole samples exhibit intense bands that were observed in the spectrum of HAp (at 500–700 cm$^{-1}$ and 900–1200 cm$^{-1}$, respectively). In particular, the bands at around 559 and 612 cm$^{-1}$ correspond mainly to the $\nu_4$ $PO_4^{3-}$ bending vibrations [47–53]. Moreover, the sharp absorption band at around 1035 cm$^{-1}$ corresponds to symmetric ($\nu_1$) and asymmetric ($\nu_3$) stretching of phosphate,

respectively, and acidic phosphate ($HPO_4^{2-}$) at about 1110 $cm^{-1}$ can be observed, which is overlapping with that from the $\nu_3$ $PO_4^{3-}$ vibration. There were also bands at around 864 and 1440 $cm^{-1}$ which originated from the carbonate ($CO_3^{2-}$) groups in the crystal lattice of the HAp [54–57], being more intense in the case of the SHAp sample, where it may be present in addition as an ionic substitute in the apatite crystal which is characteristic for a type B apatite. In the case of SHAp, a few more intense bands were observed. The band at around 941 $cm^{-1}$ can be attributed to the symmetric stretching mode ($\nu_1$) of the P–O of the phosphate group vibration mode. The band at around 729 $cm^{-1}$ could be assigned to the in-plane deformation and out-plane deformation modes of the present $CO_3^{2-}$ [58]. However, the bands between 1100 and 1250 $cm^{-1}$ may be related to impurities in an insignificant amount.

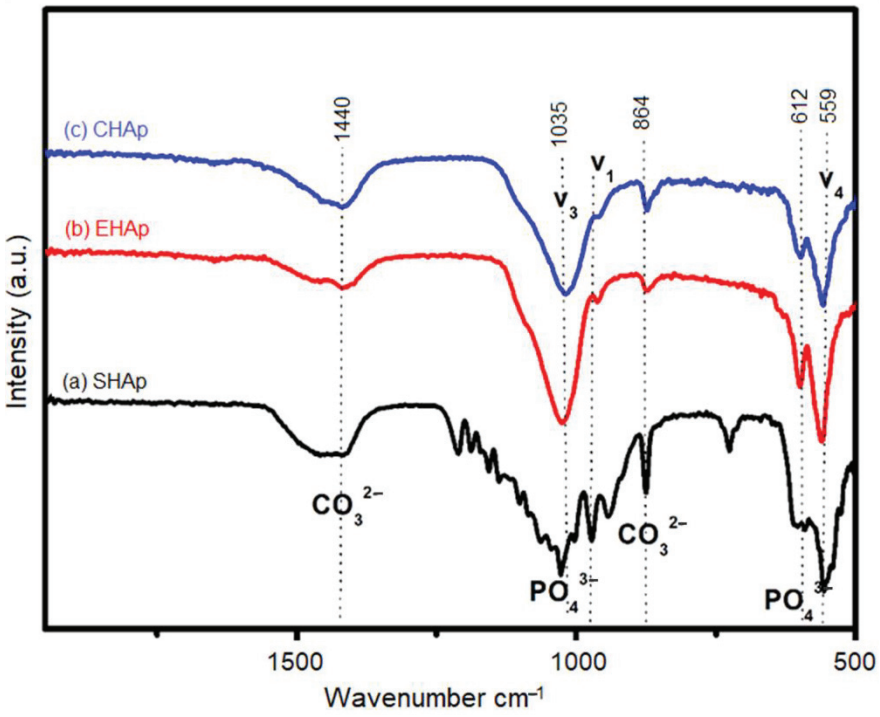


**Figure 1.** Representative FTIR spectra of (**a**) SHAp, (**b**) EHAp, and (**c**) CHAp nanoparticles.

The XRD analysis (Figure 2) of HAp samples revealed their crystal structure and crystallinity. High intensity and sharp peaks corresponding to (h k l) indices at (201), (102), (211), (300), (220), (203), (230), and (303) were obtained for the solid-state synthesized hydroxyapatite (SHAp) and revealed the formation of highly pure and crystalline SHAp according to JCPDS-861199. The XRD spectra of both sonochemical synthesized hydroxyapatites (EHAp and CHAp) show the peaks at (200), (201), (102), (211), (300), (220), (203), (230), and (303), with significant intensity in the range of 23–39° and a lower intensity at 46–63°, which may instead be consistent with the $Ca_{10}(PO_4)_6(OH)_2$ than with the $Ca_{10}(PO_4)_6OH$ phase, indicating the predominant HAp structure. The lattice parameters calculated from XRD data by the least-squares-fit method are shown in Table 1. They indicate that the values are comparable with the reported values of the a-axis (9.418 Å) and c-axis (6.884 Å) [39,59,60]. The results indicate a larger crystallite size in the case of the SHAp sample when compared to the EHAp and CHAp. This is because SHAp, prepared by solid-state reaction, is subject to precipitation and hydrolysis of calcium phosphates, causing an agglomeration during processing, consequently resulting in an increased crystallization and particle size, which is also observed in the microscopic images (Figure 3). On the other hand, the EHAp and CHAp samples exhibited relatively fine particles, which may be due to the increased amorphization of these materials during sonochemical synthesis [58].

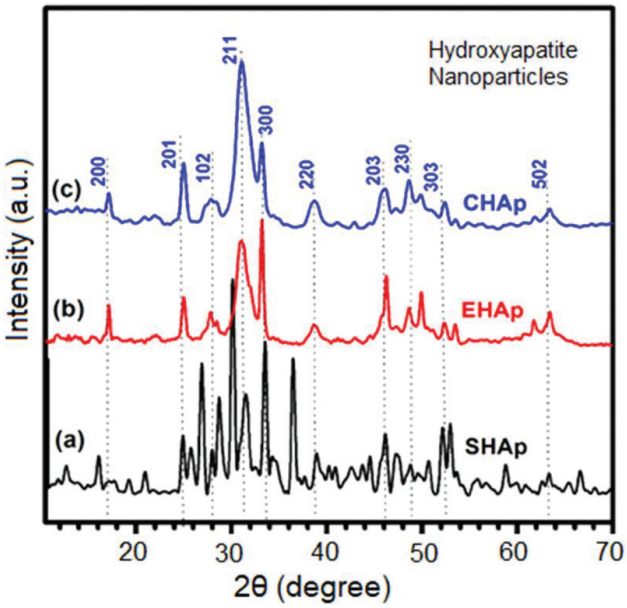


**Figure 2.** Representative XRD spectra of (**a**) SHAp, (**b**) EHAp, and (**c**) CHAp nanoparticles.

**Table 1.** Crystal structure and crystallite size of SHAp, EHAp, and CHAp nanoparticles.

| Sample | Crystal Structure | a (Å) | c (Å) | Crystallite Size (nm) |
|---|---|---|---|---|
| SHAp | Hexagonal | 11.00 | 7.00 | 10.30 |
| EHAp | Hexagonal | 10.33 | 7.11 | 7.90 |
| CHAp | Hexagonal | 9.3 | 7.10 | 5.64 |

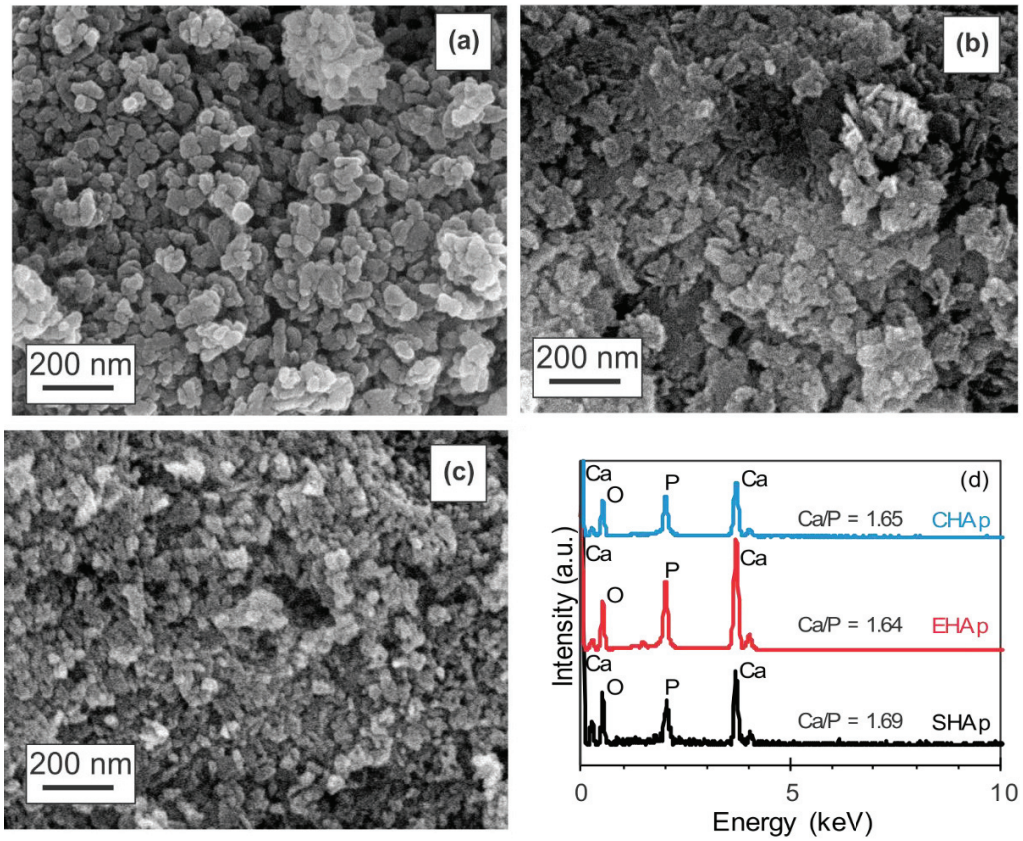


**Figure 3.** Representative SEM images of (**a**) SHAp, (**b**) EHAp, and (**c**) CHAp nanoparticles with corresponding (**d**) EDX spectra.

The SEM images of SHAp, CHAp, and EHAp samples presented in Figure 3 reveal different morphological features of the synthesized HAp. Uniformly distributed, however, relatively agglomerated and more prominent (~50 nm) SHAp nanoparticles were observed in comparison to the smaller, spherical nanocrystalline EHAp (~30 nm) and CHAp (~30–40 nm) particles produced by the sonochemical method. The ultrasound irradiation influences the chemical interactions of the reacting species, possibly by altering the rate of formation and chemical equilibrium of the calcium hydrogen phosphate phases [58]. The particle size is associated with nucleation and growth of the particles, which is related highly to the degree of supersaturation in the liquid phase. In the presence of ultrasound, the creation of microjets and the impact of shock waves influence the collapse of the microbubbles, which promotes hot spots with very high cooling rates [53] and, consequently, promotes chemical reactions and physical growth. It is also expected that the calcium phosphate being from different sources may influence the difference in particle size and morphology between the sonochemically synthesized EHAp and CHAp, as reported elsewhere [33,51]. Figure 3d shows the representative energy dispersive X-ray analysis (EDX) spectra of the samples, revealing the elemental composition of Ca and P, with the Ca/P ratio reflecting the stoichiometric structure of hydroxyapatite.

### *3.2. Mechanical Properties of Hap-Based Nanomaterials*

#### 3.2.1. Optimization of the Compression Load for Materials Preparation

In order to investigate and compare the mechanical properties of synthesized HAp powders (SHAp, EHAp, and CHAp) consolidated under high pressure, the SHAp sample was used to optimize the load applied during the pellets preparation. In that sense, the pellets were prepared by varying the applied load from 3 kN (153 MPa) to 18 kN (917 MPa) and over the range of 153–917 MPa pressure to avoid the origin of cracks and to obtain balanced mechanical properties. The maximum force, which was applied at a velocity of 0.05 mm/s, is depicted in Figure 4a. By integration of the surface below the sigma vs. epsilon diagram, the total energy ($A_{total}$) and elastic energy ($A_{elastic}$) during the pellet preparation could be obtained (Figure 4b). For each condition, 20 specimens were used, and the resultant averaged values were considered for optimizing the applied load. As shown in Figure 5, the density of HAp pellets was directly proportional to the maximal stress applied during the pellet preparation. Therefore, it can be predicted by fitting the results using the inserted equation. The hardness measurements were thus performed using the Vickers method, where diamond pyramids with angles of 136° were used, and the hardness results data were fitted as presented in Figure 6. The pellets were tested further according to the most extensively used ASTM C1424-15 (Standard Test Method for Monotonic Compressive Strength of Advanced Ceramics at Ambient Temperature) [61] to evaluate the compression test (Figure 7a). Stress vs. strain diagrams were recorded for both applied loads (Figure 7b) to define the prediction of mechanical properties. Figure 8 presents the compression strength ($\sigma_m$), fracture compression strength ($\sigma_f$), shrinkage ($A_t$), and Young's elastic modulus ($E$) by fitting the data. As shown in Figure 7b, SHAp pellets prepared with a 15 kN load are more ductile and brittle than the SHAp pellets prepared with 18 kN force. The compression strength of the SHAp pellet prepared with an 18 kN load was also higher than the 15 kN load applied to pellets of SHAp (Figure 8a) and Young's elastic modulus. Both the properties increased by increasing the pressure during the pellet preparation. However, there was a limit where some properties began to decrease, and the material started to behave in a brittle manner. The most evident property was shrinkage, which, by using high pressure during the pellet preparation, started to decrease, and the material became very brittle and impractical for further performance. Investigation of mechanical properties thus revealed that these properties could be predicted in advance.

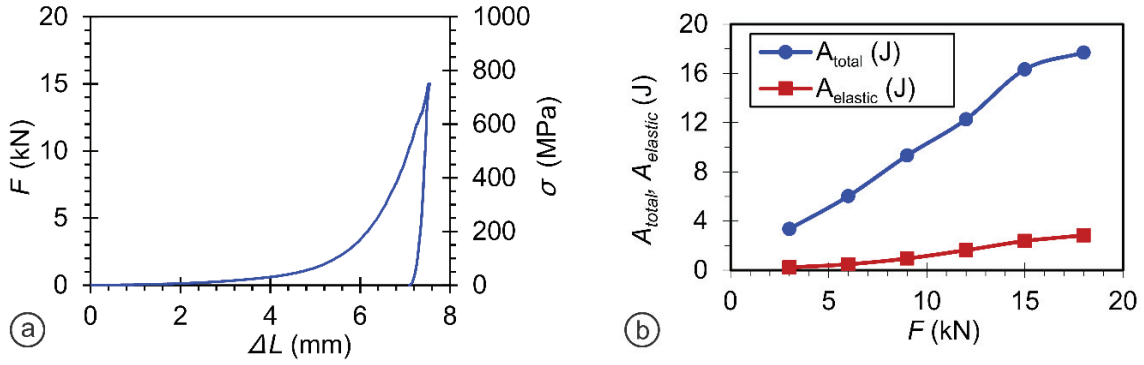


**Figure 4.** Typical graph obtained for SHAp pellet preparation by (**a**) the high-pressure compression technique, and (**b**) total and elastic specific energy for pellet preparation at different loadings.

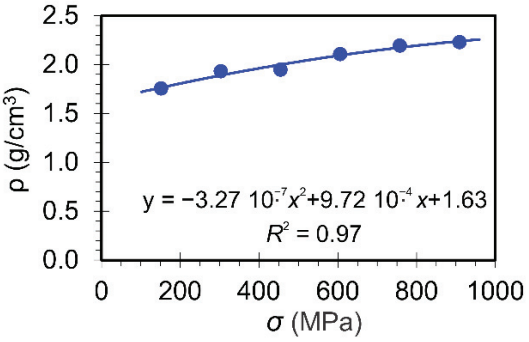


**Figure 5.** Graph showing the observed densities of SHAp pellets at different stress applied during the pellet preparation.

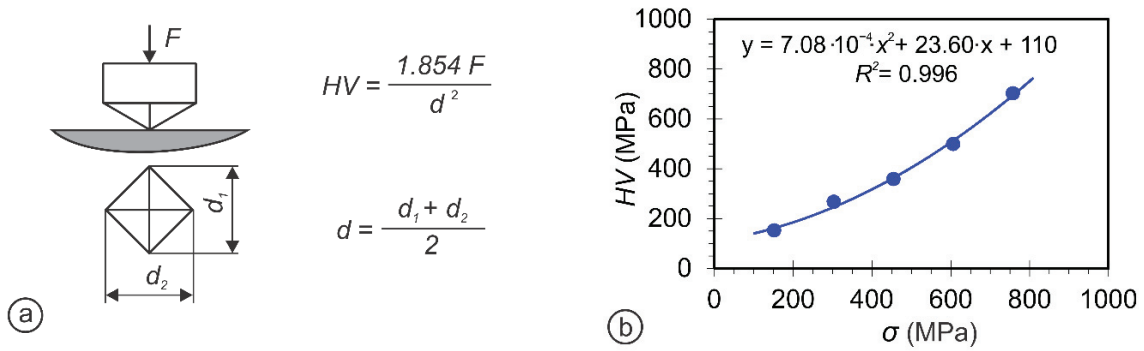


**Figure 6.** (**a**) Vickers hardness measurement method and (**b**) graph showing Vickers hardness of SHAp pellets measured as a function of load applied (150–750 MPa).

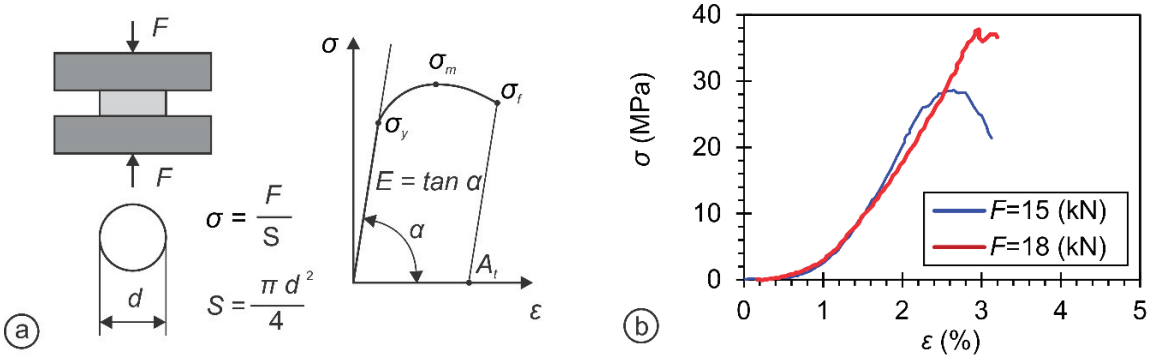


**Figure 7.** (**a**) Compression test methodology, and (**b**) stress vs. strain diagram of compression test conducted on SHAp pellets prepared with two loads applied (15 kN and 18 kN).

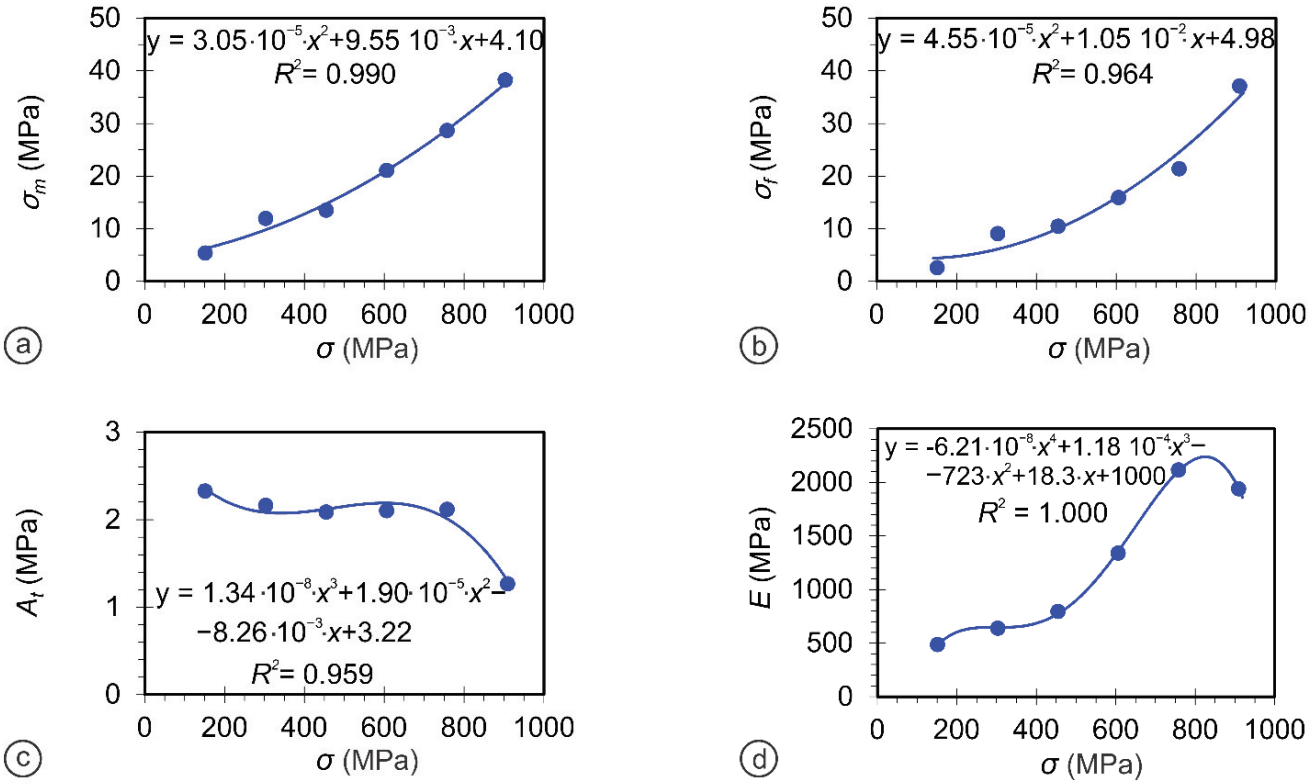


**Figure 8.** (**a**) Compression strength, (**b**) fracture compression strength, (**c**) shrinkage, and (**d**) Young's elastic modulus of SHAp pellets, depending on the stress applied (150–900 MPa) during the pellet preparation.

The pellets' fracture toughness ($K_{Ic}$) was also determined by the indentation using Vickers diamond pyramid with the angle of 136° at higher loads than at the hardness measurements to cause the crack that appeared at each corner of the indentation, as presented in Figure 9. However, as this method does not provide absolute values for fracture toughness, it measures the toughness of the material locally in the sample under a complex stress field. It can be used for comparing the fracture toughness and behavior of different materials. Therefore, the valuation of the fracture toughness was performed accordingly, based on the nature and shape of the cracks observed (Palmquist or half-penny shaped) as reported in our previous study [40,61]. If the crack in the sample was tiny and narrow, satisfying the conditions of $\frac{c}{a} \leq 2.1$, (Its correct) the Palmquist model was used to calculate fracture toughness by curve fitting when the crack was long and deep. On the other hand, the half-penny model was used when satisfying the condition $\frac{c}{a} \geq 2.1$. (Its correct) However, in more minor cracks, two cracks exist in the opposite corners in a Vickers impression as presented by the SEM image for the SHAp-based pellet (Figure 9b). Therefore, both diagonals ($2a_1$ and $2a_2$) of the indentation and crack lengths ($l_1$, $l_2$, $l_3$, and $l_4$) were measured after testing, and the fracture toughness was evaluated using Palmquist vs. half-penny model. As seen from the results in Figure 9c, the fracture toughness of SHAp pellets depends strongly on the applied stress during the pellet preparation; the lower it is, the lower is the fracture toughness. The mechanical properties of the SHAp pellet with the applied load from 3 kN (153 MPa) to 18 kN (917 MPa) were thus found to be proportional to the pressure applied during the pellet preparation.

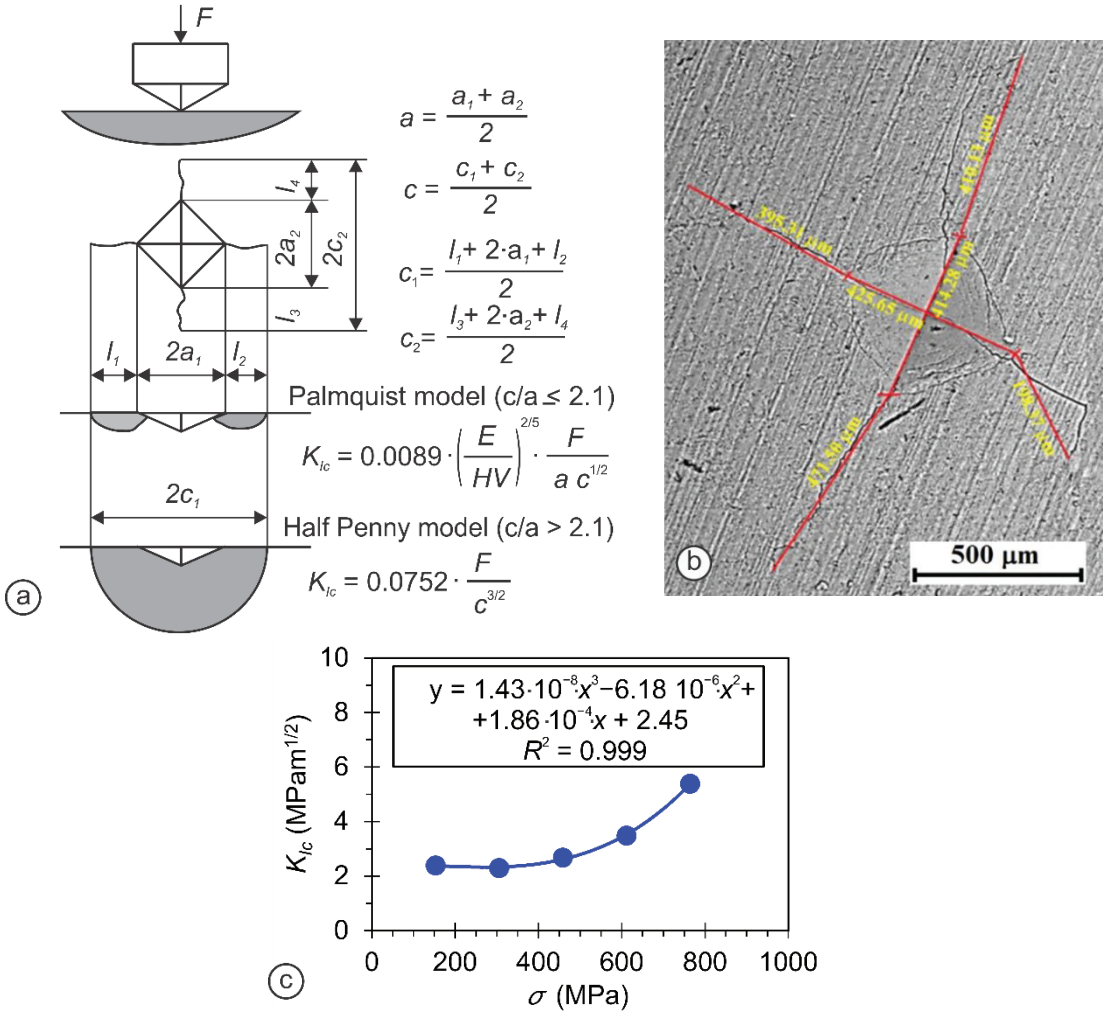


**Figure 9.** (**a**) Fracture toughness methodology, (**b**) measurement of fracture toughness by the Vickers hardness method using the data obtained from SEM imaging, and (**c**) the results of fracture toughness for the SHAp pellets depending on the stress applied (150–750 MPa) during the pellet preparation.

#### 3.2.2. Comparing the Mechanical Properties of Differently Nanostructured Materials

Biomaterials to be used as bone implants are expected to have a balanced compression strength and ductile behavior. Thus, the pellets from CHAp and EHAp nanoparticles were prepared at 15 kN (764 MPa), where the properties mentioned above are primarily balanced and compared. Total mechanical properties were measured and compared for all three Hap-based pellet materials (SHAp, EHAp, and CHAp; Figure 10).

It is believed that nanostructured ceramic can improve sinterability due to high surface energy and, therefore, improve mechanical properties. However, the sintering behavior depends on the particle size and particle size distribution, along with the fact that hard agglomerates exhibit lower densification in HAp [15]. Furthermore, different shrinkage between agglomerates is also responsible for producing small cracks in sintered HAp [40,61]. Thus, the synthesis of agglomeration-free or soft agglomerated nanostructured HAp is essential to achieve high densification and, consequently, appropriate mechanical properties.

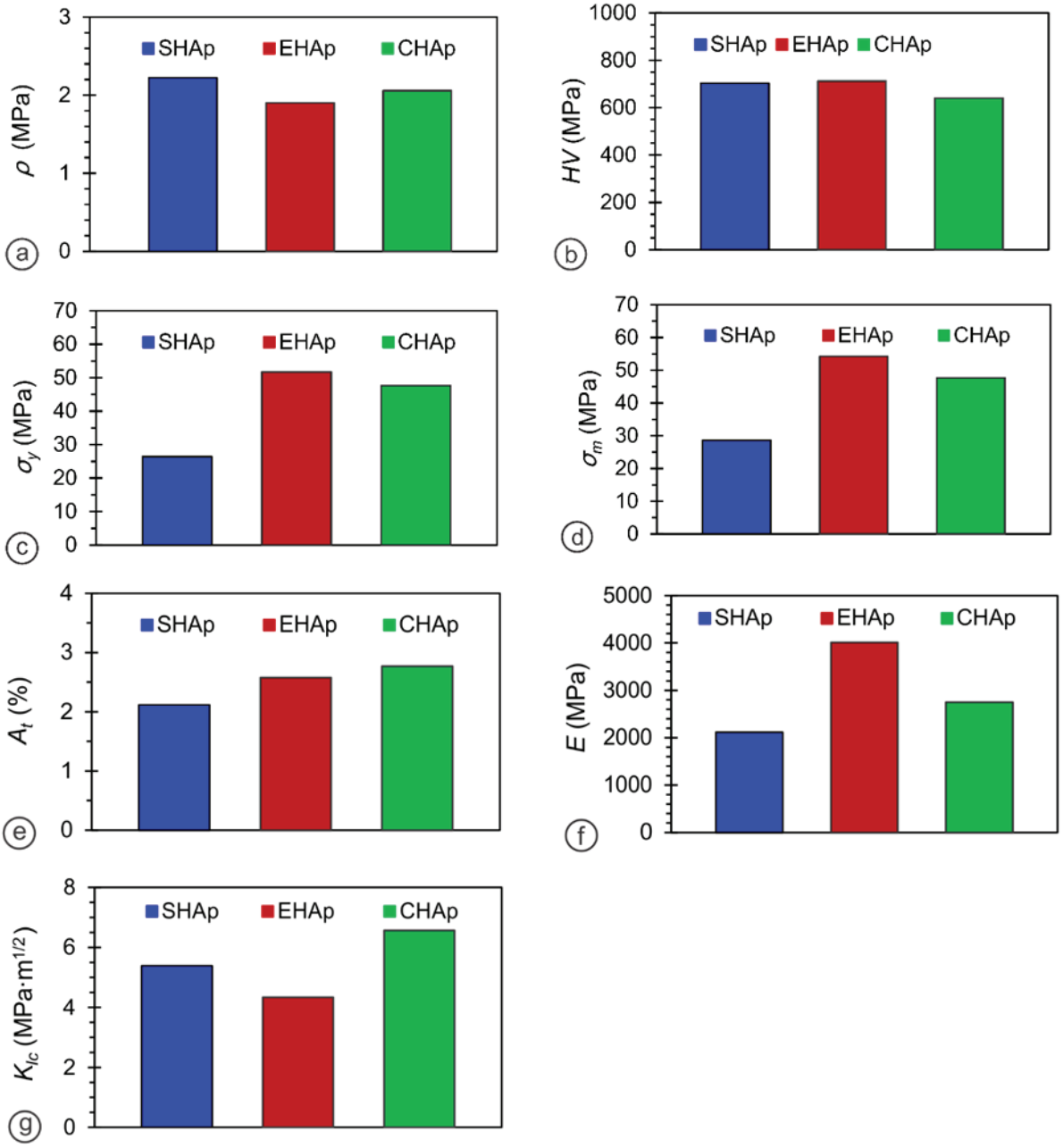


**Figure 10.** Comparative mechanical properties of SHAp-, EHAp-, and CHAp-based pellets: (**a**) Density, (**b**) hardness, (**c**) yield compression strength, (**d**) compression strength, (**e**) shrinkage, (**f**) Young's elastic modulus, and (**g**) fracture toughness. Data from at least three independent experiments are presented as mean ± SD. * $p < 0.05$ (ANOVA).

However, the density (Figure 10a) was found to be higher for the relatively more agglomerated SHAp sample (2.20 MPa) compared to the EHAp (1.89 MPa) and CHAp (2 MPa), which were similar. It may be due to different particle sizes and morphology (Figure 3) of the SHAp, leading to heterogeneity, which tends to yield spaces and imperfectly bonded boundaries known to strongly influence the mechanical properties of crystalline materials through densification [15]. At the same time, the hardness (Figure 10b) of SHAp (702 MPa) and EHAp (696 MPa) pellets was comparatively higher than the CHAp (495 MPa) sample, which may be due to the reduced porosity (void volume) and expanded contact areas between the particles, as well as the smallest crystallite size for this sample. The hardness of the material, influenced by the indentation work, was absorbed by the volume deformation processes and the fracture surface formation. The fracture generation processes need much energy, and the volume of deformation processes remains unchanged.

Besides, much lower compression strengths (Figure 10c,d) were evaluated for the SHAp pellets (26.4 MPa and 28.4 MPa), which also had an influence on lower shrinkage (2.12%; Figure 10e) and lower Young's elastic modulus (2116.75 MPa, Figure 10f), probably due to the microstructures with more vacancies, compared to the CHAp and EHAp samples. The fracture toughness (Figure 10g) was thus found to be the highest for the CHAp sample of comparatively lower mechanical strength, mainly due to the lower particle size (Figure 3) and, maybe, more spherical and smaller morphology of the HAp crystallite (Table 1, Figure 2), which do not permit its usage in load-bearing applications (44). On the other hand, the higher Young's elastic modulus (4011.1 MPa) and the lower fracture toughness (4.34 MPa $m^{1/2}$) of the EHAp sample make this material more brittle and less deformable. However, it is still higher than the other HAp bioceramics found in the literature (under 1.2 MPa $m^{1/2}$) and is comparable to the natural human bone, with a toughness of 2–12 MPa $m^{1/2}$ [15]. In this study, the Vickers hardness and indentation tests have similar meanings. The indentation method used in the Vickers hardness test is the same as the Vickers indentation method used to measure fracture toughness. In both the tests, the specimens are indented with the same indenter. However, for hardness measurements of the specimens, the diagonals of the impressions are measured to obtain Vickers hardness, whereas for fracture toughness measurements, two cracks of the impressions are also measured on a SEM microscope to obtain fracture toughness. In order to determine fracture toughness, Vickers hardness results are required for the calculations in this method. Typically, ASTM E399 is used to determine fracture [62,63] toughness by using compact tension specimens (CT) or single-edge notch bend (SENB) specimens; however, the quantity of materials was relatively small in this study. There were also issues with molding to form the desired shape. As a result, this method is feasible for performing the mechanical properties commonly used for brittle materials.

Although fracture toughness is one of the most important properties that define how an implant will resist cracking, it is also one of the most crucial safety issues of the defect. Thus, the mechanical properties of the HAp material need to be balanced to be used for specific bone graft applications. It is thus believed that the dense HAp material is expected to have a higher strength (e.g., the compression strength of 100–230 MPa for cortical bone) to resist the load [14] and to resist the high contact pressure [40]. Therefore, based on the obtained mechanical property results, the CHAp sample showed the highest capability of a material with a crack to resist fracture. Thus, it would be the most suitable material for most bone regeneration applications. On the other hand, where the yield and compression strength are essential properties, the EHAp material with 51.7 MPa and 54.5MPa, respectively, would be more appropriate, comparable to those found in the literature (Table 2, [58,63]).

**Table 2.** Comparative mechanical properties of HAp materials sintered at elevated temperatures with those prepared in the present study by uniaxial high-pressure compression at an ambient temperature and using presintered (900 °C) SHAp, EHAp, and CHAp nanoparticles.

| Samples | Preparation | Hardness (GPA) | Fracture Toughness (MPa $m^{1/2}$) | Compression Strength (MPa) | References |
|---|---|---|---|---|---|
| HAp | Sintering at 1250 °C | 5.8 | | - | [62] |
| HAp | Sintering at 1300 °C | 5.47 | 0.75 | - | [60] |
| HAp | Sintering at 1150 °C | - | - | 4.39 | [63] |
| SHAp | Uniaxial high-pressure compression at an ambient temperature | 7.02 | 5.40 | 28.40 | This study |
| EHAp | | 7.12 | 2.27 | 54.20 | This study |
| CHAp | | 6.39 | 6.57 | 47.70 | This study |

## 4. Conclusions

Nanoscale HAp bioceramics have gained attraction in biomedical applications owing to their superior biological and biomechanical properties. Therefore, the development of HAp biomedical materials will benefit from progressions in nanotechnology. The mechanical properties of HAp nanoparticles synthesized by the solid-state (SHAp) and sonochemical (EHAp and CHAp) approaches using eggshell-derived calcium hydroxide/commercial calcium hydroxide and ammonium dihydrogen orthophosphate as precursors are compared.

The mechanical properties of hydroxyapatite (HAp) nanoparticles obtained with different sizes, crystallinity, and morphology were measured in situ during high-pressure compression at a preoptimized pressure (15 kN) to assess their suitability for bone tissue regeneration applications. The smaller and more crystalline HAp nanoparticles synthesized by the sonochemical method improved the fracture toughness properties of the prepared material. At the same time, the relatively more significant and agglomerated, but homogeneously diverse, HAp particles contribute to the mechanical strength. The results indicate that the mechanical properties of composite materials obtained from HAps are dependent primarily on the properties and, secondly, on the compacting procedure. Consequently, the prepared HAp particles are promising in designing scaffolds and bone grafts for load-bearing bone regeneration applications.

**Author Contributions:** Conceptualization: A.V.G., V.K. and V.H.I.; Data curation: A.V.G., T.V., V.K. and S.S.G.; Formal analysis: V.H.I. and A.V.G.; Funding acquisition: A.V.G. and V.K.; Investigation: V.H.I., A.V.G., T.V. and V.K.; Methodology: A.V.G., V.H.I. and T.V.; Project administration: A.V.G. and V.K.; Resources: A.V.G., T.V. and V.K.; Supervision: A.V.G. and V.K.; Validation: A.V.G., V.K., V.H.I. and T.V.; Roles/Writing—original draft: V.H.I., A.V.G. and V.K.; All authors have read and agreed to the published version of the manuscript.

**Funding:** The research received no external funding.

**Data Availability Statement:** Not applicable.

**Acknowledgments:** V.H.I. is thankful to the Erasmus Mundus Project Euphrates (2013-2540/001-001-EMA2) and UGC, New Delhi, for a Research Fellowship (File No. RGNF-F1-17.1/2012-13/RGNF-2012-13-SC-MAH-35362). Furthermore, A.V.G. is thankful to Shivaji University, Kolhapur, for financial support and Shivaji University Group for Advanced Research "SUGAR" for helpful discussion.

**Conflicts of Interest:** The authors declare that they have no conflict of interest.

## References

1. Mohammadi, M.; Tulliani, J.-M.; Montanaro, L.; Palmero, P. Gelcasting and sintering of hydroxyapatite materials: Effect of particle size and Ca/P ratio on microstructural, mechanical and biological properties. *J. Eur. Ceram. Soc.* **2021**, *41*, 7301–7310. [CrossRef]
2. Hench, L.L. *An Introduction to Bioceramics*, 2nd ed.; Imperial College Press: London, UK, 2013. [CrossRef]
3. Koski, C.; Bose, S. Effects of amylose content on the mechanical properties of starch-hydroxyapatite 3D printed bone scaffolds. *Addit. Manuf.* **2019**, *30*, 100817. [CrossRef]
4. Lara-Ochoa, S.; Ortega-Lara, W.; Guerrero-Beltrán, C.E. Hydroxyapatite Nanoparticles in Drug Delivery: Physicochemistry and Applications. *Pharmaceutics* **2021**, *13*, 1642. [CrossRef] [PubMed]
5. Machado, T.R.; Leite, I.; Inada, N.; Li, M.; da Silva, J.; Andrés, J.; Beltrán-Mir, H.; Cordoncillo, E.; Longo, E. Designing biocompatible and multicolor fluorescent hydroxyapatite nanoparticles for cell-imaging applications. *Mater. Today Chem.* **2019**, *14*, 100211. [CrossRef]
6. Sheikh, Z.; Hamdan, N.; Ikeda, Y.; Grynpas, M.; Ganss, B.; Glogauer, M. Natural graft tissues and synthetic biomaterials for periodontal and alveolar bone reconstructive applications: A review. *Biomater. Res.* **2017**, *21*, 9. [CrossRef]
7. Mondal, S.; Pal, U. 3D hydroxyapatite scaffold for bone regeneration and local drug delivery applications. *J. Drug Deliv. Sci. Technol.* **2019**, *53*, 101131. [CrossRef]
8. Wang, W.; Yeung, K.W.K. Bone grafts and biomaterials substitutes for bone defect repair: A review. *Bioact. Mater.* **2017**, *2*, 224–247. [CrossRef] [PubMed]
9. Kumar, D.; Abudhahir, K.M.; Selvamurugan, N.; Vimalraj, S.; Murugesan, R.; Srinivasan, N.; Moorthi, A. Formulation and biological actions of nano-bioglass ceramic particles doped with *Calcarea phosphorica* for bone tissue engineering. *Mater. Sci. Eng. C* **2018**, *83*, 202–209. [CrossRef] [PubMed]

10. Mishra, V.K.; Bhattacharjee, B.N.; Kumar, D.; Rai, S.B.; Parkash, O. Effect of a chelating agent at different pH on the spectroscopic and structural properties of microwave derived hydroxyapatite nanoparticles: A bone mimetic material. *New J. Chem.* **2016**, *40*, 5432–5441. [CrossRef]
11. Morgan, E.F.; Unnikrisnan, G.U.; Hussein, A.I. Bone Mechanical Properties in Healthy and Diseased States. *Annu. Rev. Biomed. Eng.* **2018**, *4*, 119–143. [CrossRef] [PubMed]
12. Ferretti, J.L. Biomechanical Properties of Bone. In *Bone Densitometry and Osteoporosis*; Genant, H.K., Guglielmi, G., Jergas, M., Eds.; Springer: Berlin/Heidelberg, Germany, 1998; pp. 143–161. [CrossRef]
13. Henkel, J.; Woodruff, M.; Epari, D.; Steck, R.; Glatt, V.; Dickinson, I.C.; Choong, P.; Schuetz, M.A.; Hutmacher, D.W. Bone Regeneration Based on Tissue Engineering Conceptions—A 21st Century Perspective. *Bone Res.* **2013**, *1*, 216–248. [CrossRef] [PubMed]
14. Prakasam, M.; Locs, J.; Salma-Ancane, K.; Loca, D.; Largeteau, A.; Berzina-Cimdina, L. Fabrication, Properties and Applications of Dense Hydroxyapatite: A Review. *J. Funct. Biomater.* **2015**, *6*, 1099–1140. [CrossRef]
15. Lett, J.A.; Sagadevan, S.; Fatimah, I.; Hoque, E.; Lokanathan, Y.; Léonard, E.; Alshahateet, S.F.; Schirhagl, R.; Oh, W.C. Recent advances in natural polymer-based hydroxyapatite scaffolds: Properties and applications. *Eur. Polym. J.* **2021**, *148*, 110360. [CrossRef]
16. Lyons, J.G.; Plantz, M.A.; Hsu, W.K.; Hsu, E.L.; Minardi, S. Nanostructured Biomaterials for Bone Regeneration. *Front. Bioeng. Biotechnol.* **2020**, *8*, 922. [CrossRef] [PubMed]
17. Zhou, H.; Lee, J. Nanoscale hydroxyapatite particles for bone tissue engineering. *Acta Biomater.* **2011**, *7*, 2769–2781. [CrossRef]
18. Farokhi, M.; Mottaghitalab, F.; Samani, S.; Shokrgozar, M.A.; Kundu, S.C.; Reis, R.L.; Fatahi, Y.; Kaplan, D.L. Silk fibroin/hydroxyapatite composites for bone tissue engineering. *Biotechnol. Adv.* **2018**, *36*, 68–91. [CrossRef]
19. Shi, H.; Zhou, Z.; Li, W.; Fan, Y.; Li, Z.; Wei, J. Hydroxyapatite Based Materials for Bone Tissue Engineering: A Brief and Comprehensive Introduction. *Crystals* **2021**, *11*, 149. [CrossRef]
20. Harrison, C.; Hatton, P.; Gentile, P.; Miller, C. Nanoscale Strontium-Substituted Hydroxyapatite Pastes and Gels for Bone Tissue Regeneration. *Nanomaterials* **2021**, *11*, 1611. [CrossRef] [PubMed]
21. Liu, Y.; Lim, J.; Teoh, S.-H. Review: Development of clinically relevant scaffolds for vascularised bone tissue engineering. *Biotechnol. Adv.* **2013**, *31*, 688–705. [CrossRef] [PubMed]
22. Zhang, J.; Liu, W.; Schnitzler, V.; Tancret, F.; Bouler, J.-M. Calcium phosphate cements for bone substitution: Chemistry, handling and mechanical properties. *Acta Biomater.* **2014**, *10*, 1035–1049. [CrossRef]
23. Hendra, H.; Dadan, R.; Djuansjah, J.R.P. Metals for Biomedical Applications. In *Biomedical Engineering: From Theory to Applications*; BoD: Norderstedt, Germany, 2011. [CrossRef]
24. Dorozhkin, S.V. Calcium orthophosphate-based bioceramics and its clinical applications. In *Clinical Applications of Biomaterials. State-of-the-Art Progress, Trends and Novel Approaches*; Springer: Berlin/Heidelberg, Germany, 2017; pp. 123–226. [CrossRef]
25. Wan, C.; Chen, B. Synthesis and characterization of biomimetic hydroxyapatite/sepiolite nanocomposites. *Nanoscale* **2011**, *3*, 693–700. [CrossRef] [PubMed]
26. Cunniffe, G.M.; O'Brien, F.J.; Partap, S.; Levingstone, T.J.; Stanton, K.T.; Dickson, G.R. The synthesis and characterization of nanophase hydroxyapatite using a novel dispersant-aided precipitation method. *J. Biomed. Mater. Res. Part A* **2010**, *95*, 1142–1149. [CrossRef] [PubMed]
27. Gao, C.; Deng, Y.; Feng, P.; Mao, Z.; Li, P.; Yang, B.; Deng, J.; Cao, Y.; Shuai, C.; Peng, S. Current Progress in Bioactive Ceramic Scaffolds for Bone Repair and Regeneration. *Int. J. Mol. Sci.* **2014**, *15*, 4714–4732. [CrossRef]
28. Sadat-Shojai, M.; Khorasani, M.-T.; Dinpanah-Khoshdargi, E.; Jamshidi, A. Synthesis methods for nanosized hydroxyapatite with diverse structures. *Acta Biomater.* **2013**, *9*, 7591–7621. [CrossRef] [PubMed]
29. Barabás, R.; Czikó, M.; Dékány, I.; Bizo, L.; Bogya, E.S. Comparative study of particle size analysis of hydroxyapatite-based nanomaterials. *Chem. Pap.* **2013**, *67*, 1414–1423. [CrossRef]
30. El Briak-BenAbdeslam, H.; Mochales, C.; Ginebra, M.P.; Nurit, J.; Planell, J.A.; Boudeville, P. Dry mechanochemical synthesis of hydroxyapatites from dicalcium phosphate dihydrate and calcium oxide: A kinetic study. *J. Biomed. Mater. Res.* **2003**, *67*, 927–937. [CrossRef]
31. Pang, Y.; Bao, X. Influence of temperature, ripening time and calcination on the morphology and crystallinity of hydroxyapatite nanoparticles. *J. Eur. Ceram. Soc.* **2003**, *23*, 1697–1704. [CrossRef]
32. Zhou, Z.-H.; Zhou, P.-L.; Yang, S.; Yu, X.-B.; Yang, L.-Z. Controllable synthesis of hydroxyapatite nanocrystals via a dendrimer-assisted hydrothermal process. *Mater. Res. Bull.* **2007**, *42*, 1611–1618. [CrossRef]
33. Jevtić, M.; Mitrić, M.; Škapin, S.; Jančar, B.; Ignjatovic, N.; Uskokovic, D. Crystal Structure of Hydroxyapatite Nanorods Synthesized by Sonochemical Homogeneous Precipitation. *Cryst. Growth Des.* **2008**, *8*, 2217–2222. [CrossRef]
34. Rouhani, P.; Taghavinia, N.; Rouhani, S. Rapid growth of hydroxyapatite nanoparticles using ultrasonic irradiation. *Ultrason. Sonochem.* **2010**, *17*, 853–856. [CrossRef]
35. Giardina, M.A.; Fanovich, M.A. Synthesis of nanocrystalline hydroxyapatite from $Ca(OH)_2$ and $H_3PO_4$ assisted by ultrasonic irradiation. *Ceram. Int.* **2010**, *36*, 1961–1969. [CrossRef]
36. Kruzic, J.; Kim, D.K.; Koester, K.; Ritchie, R. Indentation techniques for evaluating the fracture toughness of biomaterials and hard tissues. *J. Mech. Behav. Biomed. Mater.* **2009**, *2*, 384–395. [CrossRef] [PubMed]

37. Wang, M.; Wang, C. Bulk Properties of Biomaterials and Testing Techniques. In *Encyclopedia of Biomedical Engineering*; Narayan, R., Ed.; Elsevier: Oxford, UK, 2019; pp. 53–64. [CrossRef]
38. Ingole, V.H.; Hussein, K.H.; Kashale, A.A.; Gattu, K.; Dhanayat, S.S.; Vinchurkar, A.; Chang, J.-Y.; Ghule, A.V. Invitro Bioactivity and Osteogenic Activity Study of Solid State Synthesized Nano-Hydroxyapatite using Recycled Eggshell Bio-waste. *Chemistry* **2016**, *1*, 3901–3908. [CrossRef]
39. Ingole, V.H.; Hussein, K.H.; Kashale, A.A.; Ghule, K.; Vuherer, T.; Kokol, V.; Chang, J.-Y.; Ling, Y.-C.; Vinchurkar, A.; Dhakal, H.; et al. Ultrasound-assisted green economic synthesis of hydroxyapatite nanoparticles using eggshell biowaste and study of mechanical and biological properties for orthopedic applications. *J. Biomed. Mater. Res. Part A* **2017**, *105*, 2935–2947. [CrossRef]
40. Ćorić, D.; Renjo, M.M.; Ćurković, L. Vickers indentation fracture toughness of Y-TZP dental ceramics. *Int. J. Refract. Met. Hard Mater.* **2017**, *64*, 14–19. [CrossRef]
41. Sakharova, N.; Fernandes, J.V.; Antunes, J.; Oliveira, M. Comparison between Berkovich, Vickers and conical indentation tests: A three-dimensional numerical simulation study. *Int. J. Solids Struct.* **2009**, *46*, 1095–1104. [CrossRef]
42. Moradkhani, A.; Baharvandi, H.; Tajdari, M.; Latifi, H.; Martikainen, J. Determination of fracture toughness using the area of micro-crack tracks left in brittle materials by Vickers indentation test. *J. Adv. Ceram.* **2013**, *2*, 87–102. [CrossRef]
43. Saranya, S.; Justin, S.J.S.; Solomon, R.V.; Wilson, P. l-arginine directed and ultrasonically aided growth of nanocrystalline hydroxyapatite particles with tunable morphology. *Colloids Surf. A Physicochem. Eng. Asp.* **2018**, *538*, 270–279. [CrossRef]
44. Al Nasim, M.N.; Li, Y.; Wen, M.; Wen, C. A review of high-strength nanolaminates and evaluation of their properties. *J. Mater. Sci. Technol.* **2020**, *50*, 215–244. [CrossRef]
45. Anstis, G.; Chantikul, P.; Lawn, B.; Marshall, D. A Critical Evaluation of Indentation Techniques for Measuring Fracture Toughness: I, Direct Crack Measurements. *J. Am. Ceram. Soc.* **1981**, *64*, 533–538. [CrossRef]
46. Kannan, S.; Lemos, A.F.; Ferreira, J.M.F. Synthesis and Mechanical Performance of Biological-like Hydroxyapatites. *Chem. Mater.* **2006**, *18*, 2181–2186. [CrossRef]
47. Liu, J.; Ye, X.; Wang, H.; Zhu, M.; Wang, B.; Yan, H. The influence of pH and temperature on the morphology of hydroxyapatite synthesized by hydrothermal method. *Ceram. Int.* **2003**, *29*, 629–633. [CrossRef]
48. Poinern, G.E.; Brundavanam, R.K.; Mondinos, N.; Jiang, Z.-T. Synthesis and characterisation of nanohydroxyapatite using an ultrasound assisted method. Ultrason. *Sonochemistry* **2009**, *16*, 469–474. [CrossRef]
49. Rusu, V.M.; Ng, C.-H.; Wilke, M.; Tiersch, B.; Fratzl, P.; Peter, M.G. Size-controlled hydroxyapatite nanoparticles as self-organized organic–inorganic composite materials. *Biomaterials* **2005**, *26*, 5414–5426. [CrossRef]
50. Morales, J.G.; Clemente, R.R.; Armas, B.; Combescure, C.; Berjoan, R.; Cubo, J.; Martínez, E.; Carmona, J.G.; Garelik, S.; Murtra, J.; et al. Controlled Nucleation and Growth of Thin Hydroxyapatite Layers on Titanium Implants by Using Induction Heating Technique. *Langmuir* **2004**, *20*, 5174–5178. [CrossRef]
51. Wang, Y.; Chen, J.; Wei, K.; Zhang, S.; Wang, X. Surfactant-assisted synthesis of hydroxyapatite particles. *Mater. Lett.* **2006**, *60*, 3227–3231. [CrossRef]
52. Kaygili, O.; Tatar, C.; Yakuphanoglu, F. Structural and dielectrical properties of Mg3–Ca3(PO4)2 bioceramics obtained from hydroxyapatite by sol–gel method. *Ceram. Int.* **2012**, *38*, 5713–5722. [CrossRef]
53. Tsai, W.; Yang, J.; Lai, C.; Cheng, Y.; Lin, C.; Yeh, C. Characterization and adsorption properties of eggshells and eggshell membrane. *Bioresour. Technol.* **2006**, *97*, 488–493. [CrossRef]
54. Xu, H.; Zeiger, B.W.; Suslick, K.S. Sonochemical synthesis of nanomaterials. *Chem. Soc. Rev.* **2013**, *42*, 2555–2567. [CrossRef]
55. Muralithran, G.; Ramesh, S. The effects of sintering temperature on the properties of hydroxyapatite. *Ceram. Int.* **2000**, *26*, 221–230. [CrossRef]
56. Forero-Sossa, P.; Olvera-Alvarez, I.; Salazar-Martinez, J.; Espinosa-Arbelaez, D.; Segura-Giraldo, B.; Giraldo-Betancur, A. Biogenic hydroxyapatite powders: Effects of source and processing methodologies on physicochemical properties and bioactive response. *Mater. Charact.* **2021**, *173*, 110950. [CrossRef]
57. Ma, D.; Wang, J.; Sun, L. Methodology for measuring fracture toughness of ceramic materials by instrumented indentation test with vickers indenter. *J. Am. Ceram. Soc.* **2017**, *16*, 695–2308. [CrossRef]
58. Huang, J.; Best, S.M. Chapter 1—Ceramic biomaterials for tissue engineering. In *Tissue Engineering Using Ceramics and Polymers*, 3rd ed.; Boccaccini, A.R., Ma, P.X., Liverani, L., Eds.; Woodhead Publishing: Cambridge, UK, 2021; pp. 3–40.
59. Arjunan, A.; Baroutaji, A.; Praveen, A.S.; Robinson, J.; Wang, C. Classification of Biomaterial Functionality. In *Encyclopedia of Smart Materials*; Olabi, A.-G., Ed.; Elsevier: Oxford, UK, 2021; pp. 86–102. [CrossRef]
60. Ramesh, S.; Tan, C.; Tolouei, R.; Amiriyan, M.; Purbolaksono, J.; Sopyan, I.; Teng, W. Sintering behavior of hydroxyapatite prepared from different routes. *Mater. Des.* **2012**, *34*, 148–154. [CrossRef]
61. Prokopiev, O.; Sevostianov, I. Dependence of the mechanical properties of sintered hydroxyapatite on the sintering temperature. *Mater. Sci. Eng. A* **2006**, *431*, 218–227. [CrossRef]
62. Khamkongkaeo, A.; Boonchuduang, T.; Klysubun, W.; Amonpattaratkit, P.; Chunate, H.-T.; Tuchinda, N.; Pimsawat, A.; Daengsakul, S.; Suksangrat, P.; Sailuam, W.; et al. Sintering behavior and mechanical properties of hydroxyapatite ceramics prepared from Nile Tilapia (*Oreochromis niloticus*) bone and commercial powder for biomedical applications. *Ceram. Int.* **2021**, *47*, 34575–34584. [CrossRef]
63. Partheniadis, I.; Papanikolaou, T.; Noisternig, M.F.; Griesser, U.J.; Kantiranis, N.; Nikolakakis, I. Structure reinforcement of porous hydroxyapatite pellets using sodium carbonate as sintering aid: Microstructure, secondary phases and mechanical properties. *Adv. Powder Technol.* **2019**, *30*, 1642–1654. [CrossRef]